Title: Room-temperature multiferroicity in all-van der Waals heterostructures

Authors: Qinqin Wang[1], Baojuan Xin[2], Chen Liu[3], Huairuo Zhang[4,5], Yinchang Ma[3], Mario Lopez[6], Hao Wu[7,8], Qishuo Tan[9], Gaojie Zhang[7,8], Haixin Chang[7,8], Xi Ling[9], Efrain E. Rodriguez[6], Albert V. Davydov[4], Xixiang Zhang[3], Wei-Hua Wang[2], Evgeny Y. Tsymbal[10], Cheng Gong[1]*

Affiliations:

[1]Department of Electrical and Computer Engineering and Quantum Technology Center, University of Maryland, College Park; MD 20742, USA.

[2]Department of Electronic Science and Engineering and Tianjin Key Laboratory of Photo-Electronic Thin Film Device and Technology, Nankai University; Tianjin 300350, China.

[3]King Abdullah University of Science and Technology (KAUST), Physical Sciences and Engineering Division (PSE); Thuwal 23955, Saudi Arabia.

[4]Materials Science and Engineering Division, National Institute of Standards and Technology (NIST), Gaithersburg; MD 20899, USA.

[5]Theiss Research, Inc., La Jolla; CA 92037, USA.

[6]Department of Chemistry and Biochemistry, University of Maryland, College Park; MD 20742, USA.

[7]Center for Joining and Electronic Packaging, State Key Laboratory of Material Processing and Die & Mold Technology, School of Materials Science and Engineering, Huazhong University of Science and Technology; Wuhan 430074, China.

[8]Wuhan National High Magnetic Field Center, Huazhong University of Science and Technology; Wuhan 430074, China.

[9]Department of Chemistry and Division of Materials Science and Engineering, Boston University, Boston; MA 02215, USA.

[10]Department of Physics and Astronomy, Nebraska Center for Materials and Nanoscience, University of Nebraska, Lincoln; NE 68588, USA.

*Corresponding author. Email: gongc@umd.edu

Abstract: Multiferroics are rare crystals of simultaneous and coupled ferroic orders, allowing disparate external stimuli to induce abrupt transformations in their structures and properties. Creating multiferroicity in two-dimensional (2D) van der Waals (vdW) platforms would invite strong quantum confinement, enhanced quasiparticle excitation, and wide property tunability to interplay, potentially engendering emergent quantum matters and phenomena. Here, we construct vdW heterostructures of Fe_3GaTe_2/$CuInP_2S_6$ to integrate ferromagnetic and ferroelectric orders. Remarkably, we observe the strong inter-ferroic coupling at room temperature, by demonstrating the ferroelectrically reconfigurable magnetic anisotropy of 2D Fe_3GaTe_2. The inter-ferroic magnetoelectricity exhibits an inversed dependence on the Fe_3GaTe_2 thickness, revealing the interfacial nature of heterostructure multiferroicity. Our discovery of all-vdW heterostructure multiferroicity opens the door to the artificial assembly of vdW layers for designer 2D multiferroics.

Main Text: Long-range orders in crystals underpin a wealth of fundamental physical properties, including ferroicity, superconductivity, and charge density waves. When multiple ferroic orders coexist in a material to form multiferroics, intriguing physical phenomena emerge owing to the complex interplay between various order parameters, leading to significantly extended device functionalities (*1-8*). An outstanding example is the magnetoelectric multiferroics that simultaneously possess ferromagnetic (FM) and ferroelectric (FE) orders, exhibiting a broad range of technologically relevant magnetoelectric, magneto-optical, and electro-optical phenomena (*2, 9-12*). Continuously thinning magnetoelectric multiferroics could eventually lead to the discovery of two-dimensional (2D) multiferroics, in which strong dimensionality effects (*13, 14*), enhanced quasiparticle excitation (*15*), and broad property tunability (*16-18*) coexist and interplay, potentially unlocking a multitude of novel physical phenomena (*19, 20*). However, despite the two decades of endeavors in chemical synthesis of ultrathin multiferroics (*21*), the resultant thin films still suffer severely from inevitable defects, lattice instability and thus degraded properties.

Unlike conventional thin-film ferroics, the recently emerged 2D van der Waals (vdW) ferroics may blaze the trail, owing to their superior crystallinity down to atomic thinness. Nevertheless, the previous efforts in searching for 2D ferromagnets and 2D ferroelectrics alone had been tremendous (*22-25*), which naturally indicates the even grander challenges in attaining a 2D layer that can embody multiple ferroic orders (i.e., the need of simultaneously overcoming the thermal fluctuations to establish 2D FM order and mitigating the depolarization fields to sustain 2D FE order) (*26, 27*). A recent study reported the discovery of single-layer vdW multiferroic NiI_2 (*8*), exhibiting a transition temperature (T_C) of 21 K, which still limits its practical applications. Given vdW layers' unprecedented freedoms in heterostructure engineering without lattice-match constraint, assembling 2D ferromagnets and 2D ferroelectrics for vdW heterostructure multiferroics may form a universally effective route to circumvent the dual challenges of simultaneously establishing two ferroic orders in one crystal (*27, 28*). The intertwined multiferroicity in vdW heterostructures, combined with the rich physical properties of their respective constituent layers such as the optical nonreciprocity of ferromagnets and optical nonlinearity of ferroelectrics, as well as the flexibility of layer stacking and twisting, could open up the extraordinary range of exotic physics and integrated functions (*29, 30*).

In this study, we design and fabricate all-vdW heterostructures of 2D FM Fe_3GaTe_2 (*31, 32*) and 2D FE $CuInP_2S_6$ (*24, 25*). Remarkably, at room temperature, we discover the robust magnetoelectric coupling between the two ferroic orders, by clearly modulating the magnetic coercivity of 2D Fe_3GaTe_2 by means of small voltages of ±6 V across the heterostructure. The modulation effects remain after the voltages are withdrawn, showcasing the clear non-volatility as the hallmark of the FE effect. The room-temperature multiferroicity in the vdW heterostructures is prominent for 2D Fe_3GaTe_2 and weakens with the increasing thickness of Fe_3GaTe_2, signifying the fundamental role of the short-range interfacial interaction underlying the inter-ferroic coupling. Our demonstration of room-temperature all-vdW multiferroic heterostructures, together with the recent advancements in vdW layer twisting and sliding, ushers in an emerging class of functional condensed matters for probing and manipulating layered magnetoelectric physics and opens up new possibilities for practical multifunctional devices in atomically thin platforms.

All-vdW multiferroic heterostructure device

We first examined the basic FE characteristics of 2D $CuInP_2S_6$ (a ferroelectric with *Tc* of ~315 K in its bulk form) (*24*) and FM characteristics of 2D Fe_3GaTe_2 (a ferromagnet with *Tc* of 350~380

K in its bulk form) (*31*) at room temperature (292 K). Piezoelectric force microscopy (PFM) was used to characterize a 4-nm-thick $CuInP_2S_6$ flake. The out-of-plane PFM phase loop of $CuInP_2S_6$ shows clear FE polarization switching (Fig. 1D) with a coercive voltage of ~1 V. Notably, the horizontal offset of the PFM phase loop from the zero bias voltage arises from the Schottky barrier difference between the upper ($CuInP_2S_6$ and the Pt/Ir conductive tip) and lower ($CuInP_2S_6$/Au electrode) interfaces of the sample (*33*). To determine the magnetic characteristics of the thin Fe_3GaTe_2 flakes, reflectance magnetic circular dichroism (RMCD) measurements were performed on a 5-nm-thick Fe_3GaTe_2 flake (Fig. 1E) at room temperature (292 K). All the RMCD measurements were carried out at 292 K, unless otherwise specified. The clear magnetic hysteresis loop with a noticeable coercive magnetic field of 42 mT confirms the room-temperature ferromagnetism in 2D Fe_3GaTe_2.

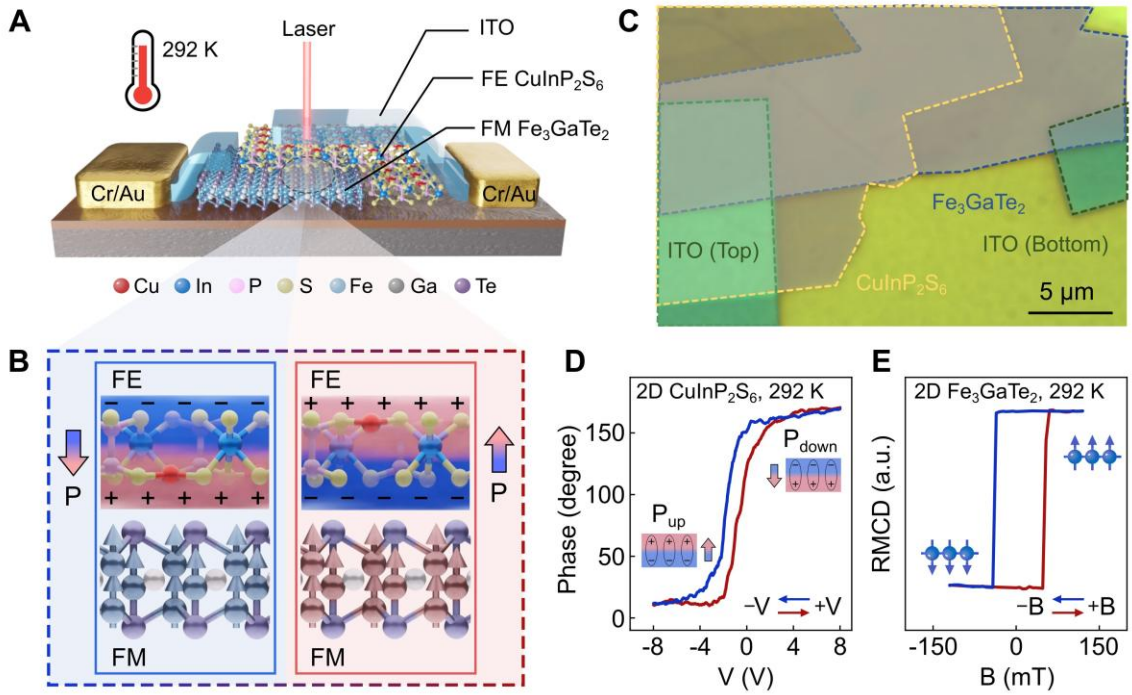

Fig. 1. All-vdW multiferroic heterostructure device. (**A**) Schematic of a room-temperature Fe_3GaTe_2/$CuInP_2S_6$ all-vdW multiferroic heterostructure device. (**B**) Lateral views of two configurations of the multiferroic heterostructure with oppositely-polarized FE $CuInP_2S_6$. When FE $CuInP_2S_6$ is oppositely polarized, the interfacial couplings differ, as indicated by the detailed interfacial atomic configurations (for instance, Cu atom (red ball) is in direct contact with FM Fe_3GaTe_2 on the left but not the right panel). As denoted by the arrows of different colors, the magnetic properties of Fe_3GaTe_2 under down- and up-polarized $CuInP_2S_6$ are different owing to distinct interfacial couplings in the two configurations. (**C**) False-color optical image of the Fe_3GaTe_2/$CuInP_2S_6$ multiferroic heterostructure device on a 260-nm-thick SiO_2/Si chip. The FM Fe_3GaTe_2 and FE $CuInP_2S_6$ flakes and ITO electrodes are circled by blue, yellow, and green dashed lines, respectively. Scale bar, 5 μm. (**D**) Out-of-plane PFM phase hysteresis loop of a 4-nm-thick $CuInP_2S_6$ flake at room temperature (292 K). Insets depict the FE polarizations of $CuInP_2S_6$ under different voltages. The clear PFM phase hysteresis loop indicates that the 2D $CuInP_2S_6$ exhibits room-temperature ferroelectricity. (**E**) Magnetic hysteresis loop of a 5-nm-thick Fe_3GaTe_2 flake characterized by RMCD at room temperature (292 K). Insets illustrate its magnetic states at different magnetic fields. The clear square-shaped magnetic hysteresis loop indicates that the 2D Fe_3GaTe_2 exhibits room-temperature ferromagnetism.

Figure 1A illustrates a vertically stacked all-vdW multiferroic heterostructure comprising 2D Fe_3GaTe_2 and 2D $CuInP_2S_6$. The 2D Fe_3GaTe_2 flakes were mechanically exfoliated from bulk crystals onto 260-nm-thick SiO_2/Si substrates. Thereafter, the 2D $CuInP_2S_6$ flakes exfoliated onto polydimethylsiloxane (PDMS) films were transferred onto the Fe_3GaTe_2 flakes to form the vdW heterostructures. The electrodes comprised a 30-nm-thick transparent indium tin oxide (ITO) bottom layer that was in direct contact with the vdW heterostructure and a top metallic contact (i.e., Cr/Au (5/50 nm)) through which voltages were applied (Methods and fig. S1). The transparent ITO electrode allowed the probing laser to access the heterostructure region for RMCD analysis. Figure 1C shows a representative false-color optical image of the $Fe_3GaTe_2/CuInP_2S_6$ multiferroic heterostructure device where the FM Fe_3GaTe_2 and FE $CuInP_2S_6$ flakes and ITO electrodes are circled by blue, yellow, and green dashed lines, respectively. The Raman spectrum (fig. S2) acquired from the heterostructure region exhibits a superposition of the vibrational modes originating from Fe_3GaTe_2 and $CuInP_2S_6$, including A_{1g} and E_{2g} modes from Fe_3GaTe_2, as well as S-P-S, cation, and P-P vibrational modes from $CuInP_2S_6$. These well-defined Raman peaks agree well with the previous works on high-quality Fe_3GaTe_2 and $CuInP_2S_6$ crystals (*34, 35*), indicating the high crystalline quality of our Fe_3GaTe_2 and $CuInP_2S_6$ flakes in heterostructures. The quality of $CuInP_2S_6$ and Fe_3GaTe_2 crystals was further examined by X-ray diffraction (XRD) measurements (fig. S3). XRD patterns of $CuInP_2S_6$ and Fe_3GaTe_2 exhibit the typical (00*l*) orientation with sharp peaks, consistent with previous reports on high-quality $CuInP_2S_6$ and Fe_3GaTe_2 crystals (*31, 33*), which confirms the superior crystalline quality of the crystals. Figure 1B shows the $Fe_3GaTe_2/CuInP_2S_6$ vdW multiferroic heterostructure for the FE polarization vector of $CuInP_2S_6$ pointing downward (P_{down}) and upward (P_{up}) (left and right panels in Fig. 1B, respectively). Under the opposite polarizations, the vertical positions of Cu^+ ions (red balls) differ in $CuInP_2S_6$, causing two distinct interfacial atomic configurations in the heterostructure: for the downward-polarized case (left panel), Cu^+ ions are relatively close to the $Fe_3GaTe_2/CuInP_2S_6$ interface, while for the upward-polarized case (right panel), Cu^+ ions are relatively away from the $Fe_3GaTe_2/CuInP_2S_6$ interface.

Ferroelectric control of 2D magnetism at room temperature

Next, we conducted RMCD measurements on the $Fe_3GaTe_2/CuInP_2S_6$ heterostructure device as the out-of-plane magnetic fields were swept under different applied voltages (Fig. 2, A and B). Figure 2A shows the magnetic field dependent RMCD under five selected voltages of +8, +4, +0 (+0 V means the withdrawal from the positive saturation voltage), -4, and -8 V during sweeping from +8 V to -8 V with a step size of 2 V. Under +8 V, the hysteresis loop exhibits a relatively small coercive magnetic field of 16 mT (defined as the OFF state) and it remains nearly unchanged when the voltage is sequentially varied to +4, +0, and -4 V. However, at -8 V, the hysteresis loop becomes noticeably larger, with a coercive magnetic field of 26 mT (defined as the ON state). Previous reports have shown that externally applied voltages can generate electric fields on magnetic materials and thus affect their magnetic properties via magnetoelectric coupling (*36, 37*). In stark contrast, for our case, the distinct hysteresis loops under ±8 V suggest that the electric field effect is not the dominant mechanism underlying our observed electrically controlled magnetic coercivities, since the opposite electric fields would be expected to cause the same effect on Fe_3GaTe_2. Subsequently, we swept the voltages from -8 V to +8 V with a step size of 2 V, and five hysteresis loops under the representative voltages are shown in Fig. 2B. When voltages of -8, -4, -0, and +4 V were applied in sequence, the four magnetic hysteresis loops exhibit the same shape and all display relatively large coercivity values of 26 mT, whereas under +8 V, the magnetic hysteresis loop returns to the smaller coercivity of 16 mT. Remarkably, when the magnetic state

is OFF (ON) at +0 V (-0 V), the shape of the magnetic hysteresis loop and the coercivity values are consistent with the previous OFF (ON) state at +8 V (-8 V), clearly indicating the non-volatility of the observed effect. The nonlinear voltage-dependent magnetic coercivity, with clear electrical non-volatility (Fig. 2C), cannot be an outcome of the pure electric field effect, but strongly highlights the FE effect on 2D magnetism (i.e., the inter-ferroic coupling) in the heterostructure. Generally, in multiferroic heterostructures, the magnetoelectric coupling may work through multiple interfacial mechanisms (e.g., interfacial strain (*38*), charge doping (*39*), and interfacial wavefunction overlap (*40*)). Specifically, in vdW systems, interfacial strain is hard to be effectively established because the layers are weakly bonded, differing from the traditional covalent-bonded composite multiferroics (*41, 42*). Our observed FE effect on 2D magnets arises primarily from other interfacial mechanisms (e.g., charge doping and interfacial wavefunction overlap), which will be discussed in more detail later.

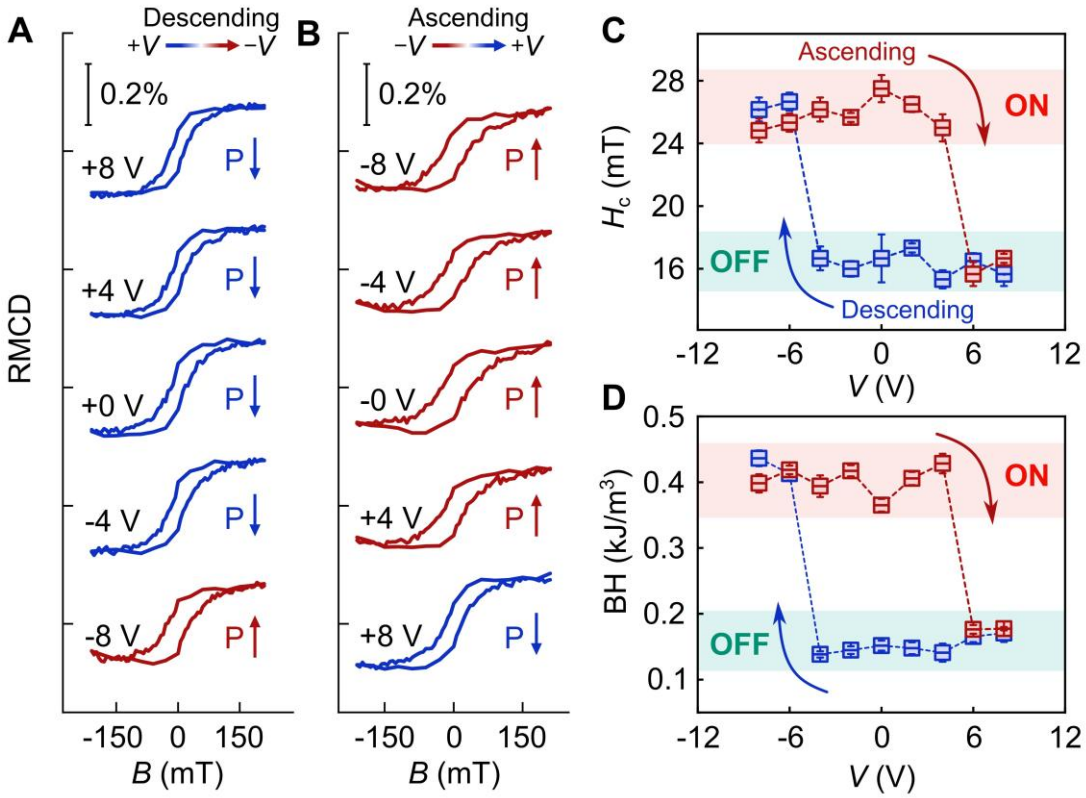

Fig. 2. Non-volatile voltage control of 2D magnetism in $Fe_3GaTe_2/CuInP_2S_6$ at room temperature. (**A** and **B**) Hysteretic magnetic field dependence of the RMCD of a 4.2-nm-thick Fe_3GaTe_2 under five selected different voltages (applied in descending order, i.e., +8, +4, +0, -4, and -8 V in (A), and ascending order in (B) at room temperature (292 K)). The hysteresis loop under +8 V exhibits a smaller coercivity of 16 mT, while under -8 V, the hysteresis loop expands to a larger coercivity of 26 mT, corresponding to two switchable magnetic states, defined as OFF and ON states here. The hysteresis loops at ±0 V (where +0 and -0 V represent the withdrawal of 0 V from positive and negative voltages, respectively) remain the same as the previous states at ±8 V, indicating non-volatile switchable multiferroicity. (**C**) Magnetic coercivity versus the applied voltage across the $Fe_3GaTe_2/CuInP_2S_6$ heterostructure. Each data point of coercivity is extracted from the magnetic hysteresis loops measured by RMCD through systematical sweeping of the voltages. The magnetic coercivity of 16 mT is obtained for the OFF state, while the larger magnetic coercivity of 26 mT is obtained for the ON state. (**D**) Maximum energy product $(BH)_{max}$ as a function of voltage. The ON and OFF states yield $(BH)_{max}$ values of 0.41 and 0.15 kJ/m^3, respectively. (C) and (D)

show similar square-shaped non-volatile hysteresis characteristics with flipping voltages of ±6 V that enable reversible switching of the two contrasting magnetic states (ON/OFF). The error bars represent the standard deviation from the mean of coercivity or $(BH)_{max}$ values derived from the magnetic hysteresis loops under three repetitive measurements.

The non-volatile FE effect on 2D magnets is also evident from the voltage-dependent maximum energy product $(BH)_{max}$ (i.e., the maximum magnetic energy that can be stored in a magnet, a critical figure of merit for a magnet's potential in energy-conversion applications such as electromechanical control and wind turbines) (*43, 44*). As shown in Fig. 2D, the $(BH)_{max}$ shows square-shaped electrical hysteresis loop. Specifically, a voltage value of -6 V is the turning point at which the magnetic state of Fe_3GaTe_2 switches to the ON state with a relatively large $(BH)_{max}$ of ~0.41 kJ/m^3. When the voltage increases to +6 V, the magnetic state switches back to the OFF state with a relatively small $(BH)_{max}$ of ~0.15 kJ/m^3. These results suggest that the switching voltages of ±6 V correspond to the two scenarios when FE $CuInP_2S_6$ is polarized upward (P_{up}) and downward (P_{down}), respectively. To further confirm that the turning points at ±6 V in voltage-dependent magnetic coercivity and $(BH)_{max}$ (Fig. 2, C and D) correspond to the occurrence of FE polarization switching, we measured the electrical tunneling resistances of the Fe_3GaTe_2/$CuInP_2S_6$/ITO trilayer junction, which can function as a ferroelectric tunneling junction (FTJ) (fig. S4). In FTJs, the polarization reversal in the FE spacer can abruptly alter the junction resistance (i.e., produce a tunneling electroresistance effect), easily by a few orders of magnitude (*35*). As shown in figure S4, the tunneling resistance indeed exhibits a hysteretic dependence on the pulse writing voltage, with three orders of magnitude change in the resistance values occurring at the turning points of ±6 V. The coincident turning points of ±6 V for switching the magnetic properties (Fig. 2, C and D) and switching the junction's electrical resistance (fig. S4D) strongly confirms that the voltage-dependent FE polarization induces our observed voltage-dependent magnetic coercivity and $(BH)_{max}$.

Ubiquitous magnetoelectric coupling across the vdW multiferroic heterostructure

Thus far, we have demonstrated the room-temperature magnetoelectric multiferroicity in all-vdW heterostructures, through non-volatile FE control of the magnetic hysteresis characteristics of 2D Fe_3GaTe_2. Considering the sensitivity of the interlayer magnetoelectric coupling to interfacial intimacy, we conducted a scanning magnetic hysteresis loop study across another similarly fabricated multiferroic heterostructure device (Fig. 3A) under opposite FE polarizations. Figure 3C shows the magnetic coercivity and $(BH)_{max}$ mappings of the 2D Fe_3GaTe_2 when $CuInP_2S_6$ is oppositely polarized (the magnetic hysteresis loops of a representative point under the two opposite polarizations of FE $CuInP_2S_6$ are plotted in Fig. 3B). Under downward polarization, Fe_3GaTe_2 exhibits relatively small magnetic coercivity in the range of 16–21 mT and low $(BH)_{max}$ values between 0.6–1.0 kJ/m^3, shown in blue in the mapping results (top panels of Fig. 3C). In contrast, when $CuInP_2S_6$ is polarized upward, Fe_3GaTe_2 exhibits relatively large coercivity values in the range of 29–34 mT and high $(BH)_{max}$ values spanning 1.6–2.0 kJ/m^3, as indicated by the red color in the bottom panels of Fig. 3C. Under opposite FE polarizations, the clear contrast in the magnetic coercivity and $(BH)_{max}$ values across the scanned region highlights that the interfacial multiferroic coupling is effectively established across the heterostructure.

We continued to demonstrate that such a magnetoelectric effect can be repetitively toggled by externally applied voltages. Figure 3B shows the reversible switching of magnetic states by periodically applying positive and negative pulse voltages. The measured hysteresis loop exhibits a magnetic coercivity of 18 mT and $(BH)_{max}$ of 0.9 kJ/m^3 (OFF state) after applying a single pulse

of +6 V voltage (with a 1 ms pulse width). An ensuing single pulse of -6 V switches the FE polarization of $CuInP_2S_6$ and causes the magnetic hysteresis loop of the Fe_3GaTe_2 with an enhanced coercivity of 29 mT and an enlarged $(BH)_{max}$ value of 1.7 kJ/m^3 (ON state). The applied pulse voltage serves as a knob to switch the FE polarization of $CuInP_2S_6$, which exerts effects on FM Fe_3GaTe_2 through inter-ferroic coupling. This is different from the previous work on electrical switching of magnetization in twist monolayer-bilayer graphene, where the pulse voltage is used to finely tune the chemical potential across the energy gap and causes magnetization reversal in orbital Chern insulators (*45*). Reversible switching between these two contrasting magnetic states does not require thermal cycles or charge current (*46*), suggesting the prospect of the energy-efficient electrical control of magnetism in our all-vdW multiferroic devices. Additional cycles of subsequent voltage pulses (Fig. 3D and fig. S5) switch the magnetic states back and forth with no obvious sign of fatigue. These testing experiments showcase that our FE switching of all-vdW multiferroic heterostructures are electrically reversible at room temperature. Figure S6 shows the endurance measurement on another $Fe_3GaTe_2/CuInP_2S_6$ multiferroic heterostructure over 3,000 cycles. Extrapolation based on the experimental data indicates that the magnetic state switching can potentially exceed 10^5 cycles without an obvious sign of fatigue.

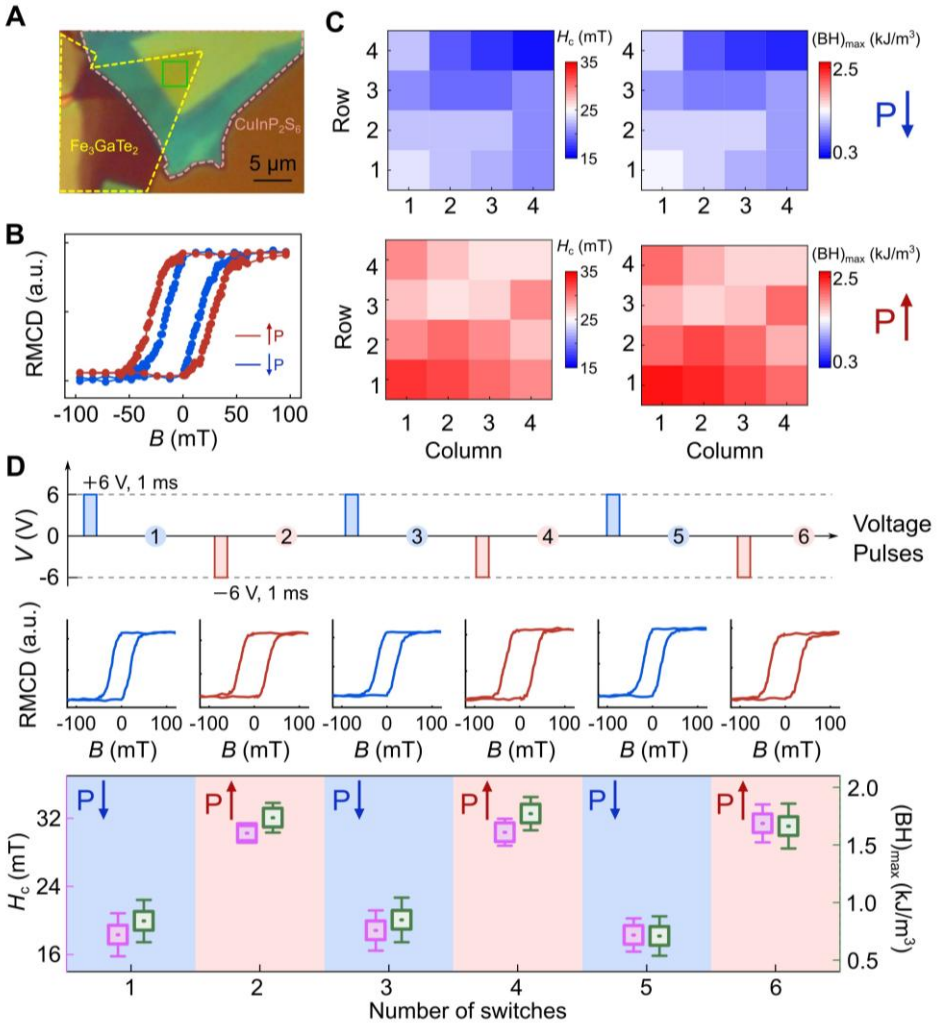

Fig. 3. Electrically togglable multiferroicity across the $Fe_3GaTe_2/CuInP_2S_6$ heterostructure. (**A**) Optical image of an $Fe_3GaTe_2/CuInP_2S_6$ multiferroic heterostructure device. The yellow and pink dashed

lines encircle the FM Fe_3GaTe_2 and FE $CuInP_2S_6$ flakes, respectively. Scale bar, 5 μm. (**B**) Magnetic hysteresis loops measured under two opposite FE polarizations (i.e., P_{down} and P_{up}). (**C**) Magnetic coercivity and $(BH)_{max}$ mappings of a 4 × 4 matrix (the distance between every measurement point corresponding to a pixel is 1 μm) within the region indicated by green rectangular box in (A) under two opposite FE polarizations. The blue (red) color map for downward (upward) polarization indicates that the interfacial multiferroic effect can be established across the heterostructure region. (**D**) Repetitive switching of the ON and OFF magnetic states by applying periodic pulse voltages. Schematic of the experimental protocol (top panel): voltage pulses of alternating polarity, V = ± 6 V, were applied sequentially, and the RMCD measurements (middle panel) were conducted after each pulse. At a positive voltage (+6 V), the hysteresis loops (in blue) exhibit small magnetic coercivities of ~19 mT, whereas at a negative voltage (-6 V), the hysteresis loops (in red) exhibit large coercivities of ~30 mT. The successive and reversible switching of magnetic states using ±6 V voltage pulses is evident in our multiferroic device. The error bars represent the standard deviation from the mean of coercivity or $(BH)_{max}$ derived from the magnetic hysteresis loops under three repetitive measurements.

Short-range interfacial nature of the inter-ferroic coupling

Finally, we studied the FE effect on FM Fe_3GaTe_2 flakes of various thicknesses. To avoid the device fabrication variance, we exfoliated a large Fe_3GaTe_2 flake comprising different thicknesses (i.e., 4, 6, 9, and 13 nm (fig. S7)) and then transferred a visually uniform $CuInP_2S_6$ flake to form a multiferroic heterostructure (inset of Fig. 4C). For the 4- and 6-nm-thick Fe_3GaTe_2 samples, as shown in Fig. 4A and Fig. 4B, the magnetic hysteresis loops exhibit smaller coercivities under the downward polarization (blue loops and bars) than under the upward polarization (red loops and bars). When the thickness of Fe_3GaTe_2 is increased to 9 nm, the hysteresis loops under the two opposite FE polarizations still exhibit a contrast, but much smaller than the cases of 4-nm and 6-nm Fe_3GaTe_2. For the 13-nm-thick Fe_3GaTe_2, the two magnetic hysteresis loops under the opposite FE polarizations of $CuInP_2S_6$ are almost identical, with magnetic coercivities of ~160 mT. To quantify the FE effect on 2D magnetism in Fe_3GaTe_2 of different thicknesses, we define control efficiency as $(H_{C1}\text{-}H_{C2})/H_{C2}$, where H_{C1} and H_{C2} represent the magnetic coercivities measured under upward and downward FE polarizations, respectively. For the 4-, 6-, 9-, and 13-nm-thick Fe_3GaTe_2 samples (Fig. 4C), the control efficiencies are 50 %, 22 %, 3 %, and 0 %, respectively. This trend of increasing control efficiencies with decreasing thickness continues down to the bilayer Fe_3GaTe_2 sample (fig. S8) (note that the monolayer Fe_3GaTe_2 has a T_C value of 240 K, well below room temperature (*47*), and thus is out the scope of this work), revealing the short-range interfacial nature of the heterostructure magnetoelectric coupling.

Generally, in multiferroic heterostructures, the inter-ferroic coupling may primarily arise from three types of interfacial interaction mechanisms: interfacial strain (*38*), charge transfer induced doping (*39, 48*), and interfacial wavefunction overlap (i.e., interfacial hybridization) (*40*). As discussed above, interfacial strain, though commonly observed in covalently bonded composite multiferroics (*41, 42*), is hard to be effectively established in vdW heterostructures of weakly bonded layers. We conducted first-principles calculations based on density functional theory to evaluate the roles of charge doping and interfacial wavefunction overlap in our observed magnetoelectric effect. Considering that both the XRD and transmission electron microscopy (TEM) characterizations on Fe_3GaTe_2 crystals suggest our crystals' high quality (figs. S3 and S9), the observed magnetic coercivity of Fe_3GaTe_2 is less likely dominated by extrinsic factors such as defects but primarily dominated by the intrinsic magnetic anisotropy energy (MAE). Our calculations reveal a small difference in charge doping levels of 6.90×10^{12} holes/cm^2 in Fe_3GaTe_2 from the adjacent $CuInP_2S_6$ layer under opposite FE polarizations (the interfacial charge transfer

for upward and downward polarizations are 1.59 × 10^{13} holes/cm^2 and 0.90 × 10^{13} holes/cm^2, respectively (fig. S10)), which represents a small amount of electron concentration modulation (*27*), typically insufficient to induce sizable changes in magnetic properties. Our calculated doping-dependent MAE confirmed that such a doping level variation in Fe_3GaTe_2 can hardly cause a sizable MAE change (fig. S10). Furthermore, our calculated differential charge density in the $Fe_3GaTe_2/CuInP_2S_6$ heterostructure with oppositely polarized FE polarizations exhibit noticeable difference in the charge redistribution induced by the interfacial wavefunction overlap (fig. S11), which suggests that the interfacial wavefunction overlap can play an important role in the observed FE effects on 2D magnetism. Essentially, when $CuInP_2S_6$ is oppositely polarized, the Cu^+ ions move close to or away from the Fe_3GaTe_2 layer (see Fig. 1B), causing different interfacial electron distributions (i.e., different interfacial crystal fields) (*27, 40, 49*) that can readily modify the magnetic anisotropy of 2D magnets.

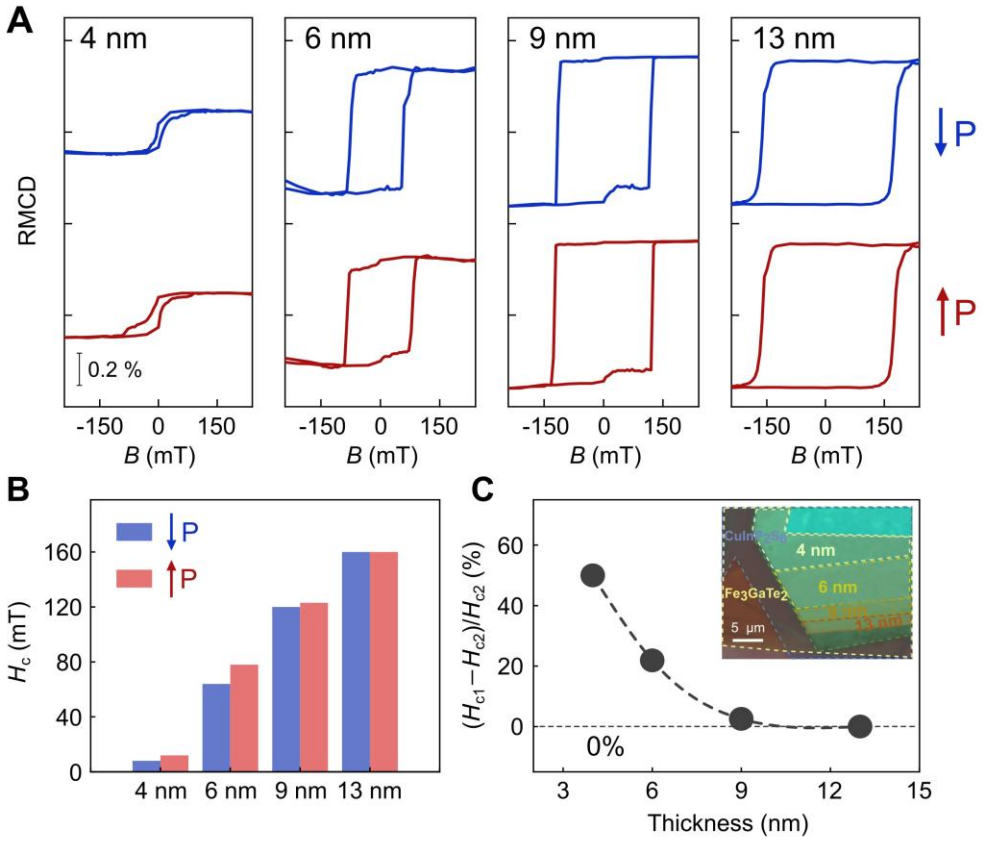

Fig. 4. The Fe_3GaTe_2 thickness dependent inter-ferroic coupling in $Fe_3GaTe_2/CuInP_2S_6$. (**A**) Hysteretic magnetic field dependence of the RMCD of a $Fe_3GaTe_2/CuInP_2S_6$ device with Fe_3GaTe_2 of various thicknesses under opposite FE polarizations. When the FE $CuInP_2S_6$ is oppositely polarized, as denoted by the blue and red arrows, the magnetic coercivities of the 4-, 6-, and 9-nm-thick Fe_3GaTe_2 change clearly (blue verse red hysteresis loops). However, for the 13-nm-thick Fe_3GaTe_2, the hysteresis loops under the two opposite polarizations are nearly identical. (**B**) Summary of the coercivities of Fe_3GaTe_2 with various thicknesses under two opposite FE polarizations. (**C**) The $(H_{C1}-H_{C2})/H_{C2}$ values measured for Fe_3GaTe_2 flakes of various thicknesses. H_{C1} and H_{C2} are the coercivities of the hysteresis loops measured under upward and downward FE polarizations, respectively. The $(H_{C1}-H_{C2})/H_{C2}$ value decreases with the increasing thickness of Fe_3GaTe_2, signifying the short-range nature of the interfacial magnetoelectric effect. Inset: a false-color optical image of the $Fe_3GaTe_2/CuInP_2S_6$ device. The FM Fe_3GaTe_2 and FE $CuInP_2S_6$ flakes are circled by blue and yellow dashed lines, respectively. The regions with Fe_3GaTe_2 of different

thicknesses are circled with from light yellow to orange dashed lines, corresponding to the increasing thickness. Fe_3GaTe_2 flakes of different thicknesses share the same uniform $CuInP_2S_6$ flake in the multiferroic device. Scale bar, 5 μm.

Conclusions

In summary, we design and fabricate vdW heterostructures of $Fe_3GaTe_2/CuInP_2S_6$ and unambiguously observe the room-temperature magnetoelectric multiferroicity. By means of small voltages of ±6 V, we electrically switch the FE polarization of 2D $CuInP_2S_6$, thereby concurrently modulating the magnetic anisotropy of 2D Fe_3GaTe_2 in a reversible and non-volatile manner. The inter-ferroic magnetoelectric effect exhibits an inversed dependence on the Fe_3GaTe_2 thickness, clearly revealing the fundamental role of the short-range interfacial coupling underlying the heterostructure multiferroicity. Together with the recent advancements in layer twisting and sliding, our discovery of room-temperature all-vdW multiferroic heterostructures potentially reshapes the landscape of functional quantum heterostructures by paving new avenues towards designer 2D multiferroics, which opens up new solid-state platforms for ultracompact magnetoelectric and magneto-optical devices.

References and Notes

1. E. Hassanpour, Y. Zemp, Y. Tokunaga, Y. Taguchi, Y. Tokura, T. Lottermoser, M. Fiebig, M. C. Weber, Magnetoelectric transfer of a domain pattern. *Science* **377**, 1109-1112 (2022).
2. N. A. Spaldin, R. Ramesh, Advances in magnetoelectric multiferroics. *Nat. Mater.* **18**, 203-212 (2019).
3. L. Ponet, S. Artyukhin, T. Kain, J. Wettstein, A. Pimenov, A. Shuvaev, X. Wang, S. W. Cheong, M. Mostovoy, A. Pimenov, Topologically protected magnetoelectric switching in a multiferroic. *Nature* **607**, 81-85 (2022).
4. J. Long, M. S. Ivanov, V. A. Khomchenko, E. Mamontova, J. M. Thibaud, J. Rouquette, M. Beaudhuin, D. Granier, R. A. S. Ferreira, L. D. Carlos, B. Donnadieu, M. S. C. Henriques, J. A. Paixao, Y. Guari, J. Larionova, Room temperature magnetoelectric coupling in a molecular ferroelectric ytterbium(III) complex. *Science* **367**, 671-676 (2020).
5. X. Qian, X. Chen, L. Zhu, Q. M. Zhang, Fluoropolymer ferroelectrics: multifunctional platform for polar-structured energy conversion. *Science* **380**, eadg0902 (2023).
6. M. Fiebig, T. Lottermoser, D. Meier, M. Trassin, The evolution of multiferroics. *Nat. Rev. Mater.* **1**, 1-14 (2016).
7. T. Han, Z. Lu, G. Scuri, J. Sung, J. Wang, T. Han, K. Watanabe, T. Taniguchi, L. Fu, H. Park, L. Ju, Orbital multiferroicity in pentalayer rhombohedral graphene. *Nature* **623**, 41-47 (2023).
8. Q. Song, C. A. Occhialini, E. Ergecen, B. Ilyas, D. Amoroso, P. Barone, J. Kapeghian, K. Watanabe, T. Taniguchi, A. S. Botana, S. Picozzi, N. Gedik, R. Comin, Evidence for a single-layer van der Waals multiferroic. *Nature* **602**, 601-605 (2022).
9. C. Gong, E. M. Kim, Y. Wang, G. Lee, X. Zhang, Multiferroicity in atomic van der Waals heterostructures. *Nat. Commun.* **10**, 2657 (2019).

10. Z. Ji, W. Liu, S. Krylyuk, X. Fan, Z. Zhang, A. Pan, L. Feng, A. Davydov, R. Agarwal, Photocurrent detection of the orbital angular momentum of light. *Science* **368**, 763-767 (2020).

11. W. Eerenstein, N. D. Mathur, J. F. Scott, Multiferroic and magnetoelectric materials. *Nature* **442**, 759-765 (2006).

12. J. T. Heron, M. Trassin, K. Ashraf, M. Gajek, Q. He, S. Y. Yang, D. E. Nikonov, Y. H. Chu, S. Salahuddin, R. Ramesh, Electric-field-induced magnetization reversal in a ferromagnet-multiferroic heterostructure. *Phys. Rev. Lett.* **107**, 217202 (2011).

13. A. Splendiani, L. Sun, Y. Zhang, T. Li, J. Kim, C. Y. Chim, G. Galli, F. Wang, Emerging photoluminescence in monolayer MoS_2. *Nano Lett*. **10**, 1271-1275 (2010).

14. K. F. Mak, C. Lee, J. Hone, J. Shan, T. F. Heinz, Atomically thin MoS_2: a new direct-gap semiconductor. *Phys. Rev. Lett*. **105**, 136805 (2010).

15. A. Rodin, M. Trushin, A. Carvalho, A. H. Castro Neto, Collective excitations in 2D materials. *Nat. Rev. Phys.* **2**, 524-537 (2020).

16. M. Zeng, J. Liu, L. Zhou, R. G. Mendes, Y. Dong, M. Y. Zhang, Z. H. Cui, Z. Cai, Z. Zhang, D. Zhu, T. Yang, X. Li, J. Wang, L. Zhao, G. Chen, H. Jiang, M. H. Rummeli, H. Zhou, L. Fu, Bandgap tuning of two-dimensional materials by sphere diameter engineering. *Nat. Mater.* **19**, 528-533 (2020).

17. H. Wang, H. Yuan, S. Sae Hong, Y. Li, Y. Cui, Physical and chemical tuning of two-dimensional transition metal dichalcogenides. *Chem. Soc. Rev.* **44**, 2664-2680 (2015).

18. Q. Li, M. Yang, C. Gong, R. V. Chopdekar, A. T. N'Diaye, J. Turner, G. Chen, A. Scholl, P. Shafer, E. Arenholz, A. K. Schmid, S. Wang, K. Liu, N. Gao, A. S. Admasu, S. W. Cheong, C. Hwang, J. Li, F. Wang, X. Zhang, Z. Qiu, Patterning-induced ferromagnetism of Fe_3GeTe_2 van der Waals materials beyond room temperature. *Nano Lett.* **18**, 5974-5980 (2018).

19. T. Zhong, X. Li, M. Wu, J. M. Liu, Room-temperature multiferroicity and diversified magnetoelectric couplings in 2D materials. *Natl. Sci. Rev.* **7**, 373-380 (2020).

20. R. Streubel, N. Kent, S. Dhuey, A. Scholl, S. Kevan, P. Fischer, Spatial and temporal correlations of XY macro spins. *Nano Lett.* **18**, 7428-7434 (2018).

21. T. Xu, T. Shimada, Y. Araki, J. Wang, T. Kitamura, Multiferroic domain walls in ferroelectric $PbTiO_3$ with oxygen deficiency. *Nano Lett.* **16**, 454-458 (2016).

22. C. Gong, L. Li, Z. Li, H. Ji, A. Stern, Y. Xia, T. Cao, W. Bao, C. Wang, Y. Wang, Z. Q. Qiu, R. J. Cava, S. G. Louie, J. Xia, X. Zhang, Discovery of intrinsic ferromagnetism in two-dimensional van der Waals crystals. *Nature* **546**, 265-269 (2017).

23. B. Huang, G. Clark, E. Navarro-Moratalla, D. R. Klein, R. Cheng, K. L. Seyler, D. Zhong, E. Schmidgall, M. A. McGuire, D. H. Cobden, W. Yao, D. Xiao, P. Jarillo-Herrero, X. Xu, Layer-dependent ferromagnetism in a van der Waals crystal down to the monolayer limit. *Nature* **546**, 270-273 (2017).

24. A. Belianinov, Q. He, A. Dziaugys, P. Maksymovych, E. Eliseev, A. Borisevich, A. Morozovska, J. Banys, Y. Vysochanskii, S. V. Kalinin, $CuInP_2S_6$ room temperature layered ferroelectric. *Nano Lett.* **15**, 3808-3814 (2015).

25. F. Liu, L. You, K. L. Seyler, X. Li, P. Yu, J. Lin, X. Wang, J. Zhou, H. Wang, H. He, S. T. Pantelides, W. Zhou, P. Sharma, X. Xu, P. M. Ajayan, J. Wang, Z. Liu, Room-temperature ferroelectricity in $CuInP_2S_6$ ultrathin flakes. *Nat. Commun.* **7**, 12357 (2016).

26. C. Gong, X. Zhang, Two-dimensional magnetic crystals and emergent heterostructure devices. *Science* **363**, eaav4450 (2019).

27. S. Liang, T. Xie, N. A. Blumenschein, T. Zhou, T. Ersevim, Z. Song, J. R. Liang, M. A. Susner, B. S. Conner, S.-J. Gong, J.-P. Wang, M. Ouyang, I. Zutic, A. L. Friedman, X. Zhang, C. Gong, Small-voltage multiferroic control of two-dimensional magnetic insulators. *Nat. Electron.* **6**, 199-205 (2023).

28. W. Sun, W. Wang, H. Li, G. Zhang, D. Chen, J. Wang, Z. Cheng, Controlling bimerons as skyrmion analogues by ferroelectric polarization in 2D van der Waals multiferroic heterostructures. *Nat. Commun.* **11**, 5930 (2020).

29. A. Nagulu, N. Reiskarimian, H. Krishnaswamy, Non-reciprocal electronics based on temporal modulation. *Nat. Electron.* **3**, 241-250 (2020).

30. Y. Shi, Z. Yu, S. Fan, Limitations of nonlinear optical isolators due to dynamic reciprocity. *Nat. Photon.* **9**, 388-392 (2015).

31. G. Zhang, F. Guo, H. Wu, X. Wen, L. Yang, W. Jin, W. Zhang, H. Chang, Above-room-temperature strong intrinsic ferromagnetism in 2D van der Waals Fe_3GaTe_2 with large perpendicular magnetic anisotropy. *Nat. Commun.* **13**, 5067 (2022).

32. W. Zhu, S. Xie, H. Lin, G. Zhang, H. Wu, T. Hu, Z. Wang, X. Zhang, J. Xu, Y. Wang, Y. Zheng, F. Yan, J. Zhang, L. Zhao, A. Patané, J. Zhang, H. Chang, K. Wang, Large room-temperature magnetoresistance in van der Waals ferromagnet/semiconductor junctions. *Chin. Phys. Lett.* **39**, 128501 (2022).

33. J. Deng, Y. Liu, M. Li, S. Xu, Y. Lun, P. Lv, T. Xia, P. Gao, X. Wang, J. Hong, Thickness-dependent in-plane polarization and structural phase transition in van der Waals ferroelectric $CuInP_2S_6$. Small **16**, e1904529 (2020).

34. H. Yin, P. Zhang, W. Jin, B. Di, H. Wu, G. Zhang, W. Zhang, H. Chang, $Fe_3GaTe_2/MoSe_2$ ferromagnet/semiconductor 2D van der Waals heterojunction for room-temperature spin-valve devices. *CrystEngComm* **25**, 1339-1346 (2023).

35. Q. Wang, T. Xie, N. A. Blumenschein, Z. Song, J. C. Kotsakidis, A. T. Hanbicki, M. A. Susner, B. S. Conner, Q. Tan, S. H. Lee, Z. Mao, X. Ling, T. Low, J.-P. Wang, A. L. Friedman, C. Gong, Extraordinary tunnel electroresistance in layer-by-layer engineered van der Waals ferroelectric tunnel junctions. *Matter* **5**, 4425-4436 (2022).

36. F. Matsukura, Y. Tokura, H. Ohno, Control of magnetism by electric fields. *Nat. Nanotechnol.* **10**, 209-220 (2015).

37. S. Jiang, J. Shan, K. F. Mak, Electric-field switching of two-dimensional van der Waals magnets. *Nat. Mater.* **17**, 406-410 (2018).

38. D. Odkhuu, N. Kioussis, Strain-driven electric control of magnetization reversal at multiferroic interfaces. *Phys. Rev. B* **97**, 094404 (2018).

39. S. I. Kim, D. H. Kim, Y. Kim, S. Y. Moon, M. G. Kang, J. K. Choi, H. W. Jang, S. K. Kim, J. W. Choi, S. J. Yoon, H. J. Chang, C. Y. Kang, S. Lee, S. H. Hong, J. S. Kim, S. H. Baek,

Non-volatile control of 2DEG conductivity at oxide interfaces. *Adv. Mater.* **25**, 4612-4617 (2013).

40. C. G. Duan, S. S. Jaswal, E. Y. Tsymbal, Predicted magnetoelectric effect in Fe/$BaTiO_3$ multilayers: ferroelectric control of magnetism. *Phys. Rev. Lett.* **97**, 047201 (2006).
41. A. N. Buditama, K. Fitzell, D. Chien, C. Ty Karaba, S. K. Patel, H. Y. Kang, J. P. Chang, S. H. Tolbert, Strain transfer in porous multiferroic composites of $CoFe_2O_4$ and $PbZr_xTi_{1-x}O_3$. *Appl. Phys. Lett.* **120**, 192902 (2022).
42. S. K. Patel, D. D. Robertson, S. S. Cheema, S. Salahuddin, S. H. Tolbert, In-Situ Measurement of Magnetoelectric Coupling and strain transfer in multiferroic nanocomposites of $CoFe_2O_4$ and $Hf_{0.5}Zr_{0.5}O_2$ with residual porosity. *Nano Lett.* **23**, 3267-3273 (2023).
43. W. B. Cui, Y. K. Takahashi, K. Hono, $Nd_2Fe_{14}B$/FeCo anisotropic nanocomposite films with a large maximum energy product. *Adv. Mater.* **24**, 6530-6535 (2012).
44. O. Gutfleisch, M. A. Willard, E. Bruck, C. H. Chen, S. G. Sankar, J. P. Liu, Magnetic materials and devices for the 21st century: stronger, lighter, and more energy efficient. *Adv. Mater.* **23**, 821-842 (2011).
45. H. Polshyn, J. Zhu, M. A. Kumar, Y. Zhang, F. Yang, C. L. Tschirhart, M. Serlin, K. Watanabe, T. Taniguchi, A. H. MacDonald, A. F. Young, Electrical switching of magnetic order in an orbital Chern insulator. *Nature* **588**, 66-70 (2020).
46. C. K. Safeer, E. Jue, A. Lopez, L. Buda-Prejbeanu, S. Auffret, S. Pizzini, O. Boulle, I. M. Miron, G. Gaudin, Spin-orbit torque magnetization switching controlled by geometry. *Nat. Nanotechnol.* **11**, 143-146 (2016).
47. M. Wang, B. Lei, K. Zhu, Y. Deng, M. Tian, Z. Xiang, T. Wu, X. Chen, Hard ferromagnetism in van der Waals Fe_3GaTe_2 nanoflake down to monolayer. *npj 2D Mater. Appl.* **8**, 22 (2024).
48. C. G. Duan, J. P. Velev, R. F. Sabirianov, Z. Zhu, J. Chu, S. S. Jaswal, E. Y. Tsymbal, Surface magnetoelectric effect in ferromagnetic metal films. *Phys. Rev. Lett.* **101**, 137201 (2008).
49. M. K. Niranjan, J. P. Velev, C.-G. Duan, S. S. Jaswal, E. Y. Tsymbal, Magnetoelectric effect at the Fe_3O_4/$BaTiO_3$(001) interface: a first-principles study. *Phys. Rev. B* **78**, 104405 (2008).
50. G. Kresse, J. Furthmuller, Efficient iterative schemes for ab initio total-energy calculations using a plane-wave basis set. *Phys. Rev. B* **54**, 11169-11186 (1996).
51. J. Moellmann, S. Grimme, DFT-D3 Study of Some Molecular Crystals. *J. Phys. Chem. C* **118**, 7615-7621 (2014).
52. Y. Deng, Y. Yu, Y. Song, J. Zhang, N. Z. Wang, Z. Sun, Y. Yi, Y. Z. Wu, S. Wu, J. Zhu, J. Wang, X. H. Chen, Y. Zhang, Gate-tunable room-temperature ferromagnetism in two-dimensional Fe_3GeTe_2. *Nature* **563**, 94-99 (2018).
53. Y.-P. Wang, X.-Y. Chen, M.-Q. Long, Modifications of magnetic anisotropy of Fe_3GeTe_2 by the electric field effect. *Appl. Phys. Lett.* **116**, 092404 (2020).
54. H. Chen, Q. Qiao, M. S. Marshall, A. B. Georgescu, A. Gulec, P. J. Phillips, R. F. Klie, F. J. Walker, C. H. Ahn, S. Ismail-Beigi, Reversible modulation of orbital occupations via an interface-induced polar state in metallic manganites. *Nano Lett.* **14**, 4965-4970 (2014).

55. R. Li, J. Jiang, W. Mi, H. Bai, Ferroelectric polarization tailored interfacial charge distribution to modify magnetic properties of two-dimensional Janus FeBrI/In_2S_3 heterostructures. *Appl. Phys. Lett.* **120**, 162401 (2022).

56. B. Cui, C. Song, H. Mao, H. Wu, F. Li, J. Peng, G. Wang, F. Zeng, F. Pan, Magnetoelectric coupling induced by interfacial orbital reconstruction. *Adv. Mater.* **27**, 6651-6656 (2015).

Acknowledgments: B.X. and W.H.W. acknowledge the Supercomputing Center of Nankai University for the computational resources and technical support. A.V.D. acknowledge support from the Material Genome Initiative funding allocated to NIST. Disclaimer: Certain commercial equipment, instruments, software, or materials are identified in this paper in order to specify the experimental procedure adequately. Such identifications are neither intended to imply recommendation or endorsement by NIST, nor to imply that the materials or equipment adopted in this work are necessarily the best available for the study.

Funding:

Air Force Office of Scientific Research Award FA9550-22-1-0349 (C.G., Q.W.)

Naval Air Warfare Center Aircraft Division Award N00421-22-1-0001 (C.G.)

Army Research Laboratory Cooperative Agreement W911NF-19-2-0181 (C.G.)

National Science Foundation Awards DMR-2340773 and DMR-2326944 (C.G.)

U.S. Department of Energy, Office of Science, Basic Energy Sciences, grant no. DE-SC0023140 (E.Y.T.)

Science and Technology Innovation Teams of Shanxi Province Grant 202204051001002 (B.X., W.H.W.)

U.S. Department of Commerce, NIST Award 70NANB22H101 (H.Z.)

National Key Research and Development Program of China 2022YFE0134600 (H.C.)

National Natural Science Foundation of China Grants 52272152, 62174151, 61674063 and 62074061 (H.C.)

Author contributions:

C.G. conceived and supervised the project. Q.W. fabricated devices and performed the RMCD measurements under the supervision of C.G. B.X. performed the DFT calculations under the supervision of W.H.W. C.L. carried out XRD measurements of Fe_3GaTe_2 crystals and performed top-view TEM measurements of Fe_3GaTe_2 crystals under the supervision of X.Z. H.Z. and A.V.D. performed cross-sectional TEM measurements of Fe_3GaTe_2 crystals. Y.M. performed PFM measurements and analysis under the supervision of X.Z. M.L. synthesized the bulk Fe_3GaTe_2 crystals under the supervision of E.E.R., and H.W. and G.Z. synthesized the bulk Fe_3GaTe_2 crystals under the supervision of H.C. Q.T. synthesized $CuInP_2S_6$ crystals under the supervision of X.L. E.Y.T. participated in the discussion of the experimental results and provided expertise in DFT calculations. Q.W. and C.G. analyzed the data. Q.W. and C.G. wrote the manuscript. All authors commented on the manuscript.

Competing interests: The authors declare no competing interests.

Data and materials availability: All data are available in the main text or the supplementary materials.

Supplementary Materials

Materials and Methods

Figs. S1 to S11

References (*31,33–35, 47, 50–56*)